



THE AMERICAN SOCIETY OF MECHANICAL ENGINEERS
345 E. 47th St., New York, N.Y. 10017

96-GT-550

The Society shall not be responsible for statements or opinions advanced in papers or discussion at meetings of the Society or of its Divisions or Sections, or printed in its publications. Discussion is printed only if the paper is published in an ASME Journal. Authorization to photocopy material for internal or personal use under circumstance not falling within the fair use provisions of the Copyright Act is granted by ASME to libraries and other users registered with the Copyright Clearance Center (CCC) Transactional Reporting Service provided that the base fee of \$0.30 per page is paid directly to the CCC, 27 Congress Street, Salem MA 01970. Requests for special permission or bulk reproduction should be addressed to the ASME Technical Publishing Department.

Copyright © 1996 by ASME

All Rights Reserved

Printed in U.S.A.

TWO-DIMENSIONAL COMPUTATIONAL MODEL FOR WAVE ROTOR FLOW DYNAMICS



Gerard E. Welch
U.S. Army Research Laboratory
Vehicle Propulsion Directorate
NASA Lewis Research Center
Cleveland, Ohio 44135, U.S.A.

ABSTRACT

A two-dimensional (θ, z) Navier-Stokes solver for multi-port wave rotor flow simulation is described. The finite-volume form of the unsteady thin-layer Navier-Stokes equations are integrated in time on multi-block grids that represent the stationary inlet and outlet ports and the moving rotor passages of the wave rotor. Computed results are compared with three-port wave rotor experimental data. The model is applied to predict the performance of a planned four-port wave rotor experiment. Two-dimensional flow features that reduce machine performance and influence rotor blade and duct wall thermal loads are identified. The performance impact of rounding the inlet port wall, to inhibit separation during passage gradual opening, is assessed.

INTRODUCTION

The wave rotor is a machine designed to efficiently transfer energy between gas streams of differing energy density. The energy exchange is accomplished within shrouded rotor passages (see Fig. 1) by axially-propagating shock and expansion waves. The waves are initiated as the ends of the wave rotor passages open and close to the relatively steady flows in stationary inlet and outlet ports in a timed sequence set by the rotor speed and the tangential positions of the port walls. Various wave rotor cycles can be achieved by varying the sequence of passage charging and discharging events dictated by the wave timing. These include three-port divider cycles (Kentfield, 1969 and Wilson and Fronek, 1993) and four-port cycles (e.g., Mathur, 1985, Moritz, 1985, and Zauner et al., 1993) which promise attractive specific fuel consumption and specific power improvements in gas turbine engines (e.g., see Taussig, 1984 and Welch et al., 1995). The interesting history of the wave rotor and its applications has been documented elsewhere (see, for example, Azoury, 1965-66, Rose, 1979, Taussig and Hertzberg, 1984, and Shreeve and Mathur, 1985).

Wave rotor performance depends in part on proper wave timing. The asymmetric opening and closing of the rotor passages to the port flows reduce effective one-dimensional wave speeds (e.g., see Paxson,

1993) and significantly influence the shape and subsequent distortion of contact discontinuities within the rotor (cf. Eidelman, 1985). Machine performance is degraded by viscous, heat transfer, and shock losses within the rotor passages, leakage to and from the rotor passages and ports, and mixing of nonuniform port flow fields and at gas/gas interfaces. Arguably, the gas dynamic wave timing can be modeled either analytically or by the method-of-characteristics (e.g., see Burri, 1958); however, the inherent multi-dimensionality and nonlinearity of many of the wave rotor loss mechanisms provide impetus for applying computational fluid dynamics (CFD) methods to simulate the wave rotor flow dynamics.

One-dimensional (1-D), single rotor passage, CFD models (e.g., see Zehnder, 1971, Thayer et al., 1980, Wen and Mingzheng, 1982, Taussig, 1984, and Paxson, 1995) that use time-varying boundary conditions to represent the inlet and outlet port conditions accurately predict the gas dynamics within straight rotor passages having aspect (length-to-width) ratios typical of pressure exchangers (i.e., ≥ 10). Given properly calibrated loss models, the 1-D solvers can also accurately simulate machine performance. Multi-dimensional CFD models have to date assumed inviscid flow. These include single passage, two-dimensional solvers for (r, z)-coordinates (Hong-De, 1983 and Zhang, 1988) and (θ, z)-coordinates (Eidelman, 1985) and a single passage, 3-D (r, θ, z) solver (Larosiliere, 1995). Lear and Candler (1993) proposed a 2-D Euler solver which assumes 1-D flow in infinite aspect ratio rotor passages and 2-D (θ, z) steady-state flow in multiple ports. It is the understanding of the author that a 2-D (θ, z) code for unsteady, inviscid flow in multiple passages and ports has been developed by A. L. Ni of the Moscow Academy of Science (private communication, A. Pfeffer and R. Althaus, Asea-Brown-Boveri, 1994).

The CFD model described in this work addresses a need to simulate inherently two-dimensional flow features routinely encountered in the stator/rotor/stator configuration of multi-port wave rotors. These include viscous phenomena such as flow separation (e.g.,

**Presented at the International Gas Turbine and Aeroengine Congress & Exhibition
Birmingham, UK — June 10-13, 1996**

**This paper has been accepted for publication in the Transactions of the ASME
Discussion of it will be accepted at ASME Headquarters until September 30, 1996**

off the stator end-wall during rotor passage opening and closing, off the trailing edge of rotor blades, and in shock/boundary layer interactions) and inviscid phenomena such as Rayleigh-Taylor flows (including shock/contact and fan/contact interactions), gas dynamic waves emitted from the rotor passages into the ports, and passage-to-passage flow recirculation via the inlet and outlet ports. An overview of the computational model is first provided. Computed results are then compared with three-port experimental data. Finally, the model is applied to a planned four-port wave rotor experiment both to predict machine performance and to identify flow features that influence machine design and performance.

COMPUTATIONAL MODEL

The multi-region geometry and important fluid dynamic features of the wave rotor may be appreciated by considering the passage charging problem shown in Fig. 2. In this view (looking radially-inward), the wave rotor passages are unwrapped from the periphery of the rotor. The rotor passages gradually open (and close) to the inlet port as dictated by the rotor speed and the passage width. As the low pressure fluid in a rotor passage is first exposed to the high total pressure inlet port flow, compression waves move into the rotor passage, compress and set into motion the on-board "driven fluid," and thus allow the inlet port "driver" fluid to enter the rotor passage. Simultaneously, an expansion wave moves into the inlet port region and reduces the total pressure and total temperature of the entering driver fluid. In general, temperature and density are discontinuous at the distorted interface of the driver and driven gases. The right moving compression wave steepens into a shock wave which then reflects off the right-hand wall. The reflected (lambda) shock moves leftward, interacts with the established boundary layer, and compresses the driven and driver gases. The contact is significantly distorted by vorticity deposited along the contact by the reflected shock. Richtmyer-Meshkov (or shock-excited Rayleigh-Taylor) instability theory suggests that the contact distortion scales with the density difference and the strength of the shock (e.g., see Sturtevant, 1987). The inlet port is designed so that the rotating passages close just as the reflected shock reaches the rotor/port interface. The reflected shock wave is emitted into the inlet port. The gradual closing of the passage generates a pair of counter-rotating vortices.

Model Restrictions

Centripetal forces establish a tangential baroclinic torque along contact discontinuities (interfaces) between gases of differing density; this can cause significant interface skewing (cf. Keller, 1994). The distortion is expected to scale with the square of rotor Mach number and the rotor hub-to-tip ratio (cf. Larosiliere, 1995). Optimum rotor Mach numbers based on peak cycle temperature are low (≤ 0.3) and optimum hub-to-tip ratios are likely at or above 2/3 (cf. Welch, 1996); centripetal and Coriolis forces are neglected in this work and the rotor passages and inlet ports are solved at passage mid-span, in $z-\theta$ (or $x-y$) coordinates. Leakage flows, both from the rotor passages to the space between the rotor and the outer casing and from passage-to-passage, are neglected in this work. In practice leakage is mitigated by minimizing rotor/end-wall clearance and/or by using seals; however, it is noted that leakage substantially reduces the performance (e.g., see Wilson and Fronek, 1993), and can impact the radial and tangential port flow profiles, of some machines. Fluid-to-wall heat transfer is

another potentially significant loss mechanism neglected in the present work in which the passage walls are adiabatic.

The inlet port flow fields in many applications are likely turbulent. The character (laminar, transitional, or turbulent) of the boundary layer flow within the rotor passages is not known, but will certainly be influenced by the turbulence intensity of the incoming driver flow. The viscous flow of this work is modeled using laminar transport properties, under the thin-layer approximation (cf. Baldwin and Lomax, 1978). Turbulence-enhanced mixing (e.g., at gas/gas interfaces and in nonuniform outflow port flow fields) and turbulence-enhanced diffusion (e.g., of vorticity and heat) are neglected. Assessing the impact of neglecting the streamwise diffusion terms by the thin-layer approximation remains for future work.

Solution Method

The wave rotor flow field is modeled by the 2-D, unsteady, compressible, thin-layer Navier-Stokes equations with laminar viscosity. The gas is assumed calorically and thermally perfect. The finite-volume form of the governing equations are integrated in time using a second-order accurate explicit four-stage Runge-Kutta scheme (Jameson et al., 1981). The time step is dictated by the grid resolution and the CFL number, nominally set at 1.5. In the cell-centered finite-volume formulation used, the inviscid and viscous flux vectors are calculated at the cell interfaces defined by lines connecting the grid points. The inviscid flux vectors are computed using a multi-dimensional, boundary-fitted (ξ, η) coordinates formulation (Grossman and Walters, 1989 and Walters and Thomas, 1989) of Roe's (1981) approximate Riemann solution scheme with the entropy condition fix of Harten and Hyman (1983). The "left" and "right" states of the Riemann problem are set by MUSCL interpolation (van Leer, 1979) with Mulder limiting (cf. Anderson et al., 1986). In general, four grid-aligned cells are involved in the interpolation for each cell face value, so that an inviscid spatial flux derivative involves a five cell stencil and is at least second-order accurate. The shear stress and heat flux components of the viscous flux vector are central-differenced at the cell interfaces using the primitive variables of the adjacent cells and transport properties evaluated at the arithmetic mean of the static temperatures in the adjacent cells. The overall method is second-order accurate in space and time.

Port/Rotor Interfaces

The multiple rotor passages are solved on identical grid blocks. At the beginning of each time step, the rotor grids are advanced according to the current time step and the rotor linear speed. A schematic diagram of the interface at the left end of the rotor at some arbitrary time is provided in Fig. 3. The interface is represented by a zone in which zero volume cells are artificially created by the overlapping of constant- η grid lines from the left and right grid blocks. This definition ensures that each interior cell communicates with an integer number of artificial interface cells. The left and the right face of each interface cell are set by the MUSCL interpolation, where now the four point stencil involves both the left and right grid blocks. For example, the interpolation for the primitive variables at the left face of an interface cell involves two interior cells of the left grid block and one interior cell of the right block. Likewise, the interpolation for the primitive variables at the right face of the grid block involves two

points in the right grid block and one in the left. In the case where one or more of the interface cell faces is a wall (e.g., a stator surface or a rotor blade), the wall boundary conditions described in the following section are imposed. If both interface cell faces are walls, interpolation is not required; i.e., that interface cell does not affect any interior cell. After the left and right faces of the artificial interface cells are set, an approximate Riemann solution provides the primitive variables and fluxes at the interface. For a given interior cell, the product of the inviscid flux times cell area is obtained by summing the flux/area products of the integer number of interface cells that correspond to that interior cell. For example, if the interior cell in the right grid block is spanned by three interface cells, the flux/area product values for the three interface cells are summed and the total flux/area product is applied at the left face of the interior cell. In this way overall flux conservation is imposed by the interface routine at the beginning of each time step.

Port Boundary Conditions

Phantom cells are used to impose subsonic boundary conditions at the inlet port inflow boundary and at the exhaust port outflow boundary. Standard 1-D characteristics boundary conditions are used in which the Riemann variables are based on the streamwise covariant velocity component. The normal derivative of pressure and the normal velocity component are required to be zero at walls. In inviscid computations, the streamwise covariant velocity component is allowed to slip at the wall. In viscous computations, phantom cells internal to walls are used to ensure that the streamwise covariant velocity component and the normal derivative of temperature are zero at the wall. The local wall temperature itself is therefore very nearly the fluid temperature in the adjacent cell, and can be inferred at any time.

Chima's (1987) single-block quasi-3-D rotor viscous code (RVCQ3D) provided a skeletal structure for the multi-block (WROTOR2D) solver described above. Earlier papers (Welch, 1993 and Welch and Chima, 1993) have presented detailed descriptions of the CFD model, examples of code validation, and applications to wave rotor passage charging processes (e.g., that shown in Fig. 2).

DIVIDER CYCLE EXPERIMENT COMPARISON

Three-port divider cycles divide a medium stagnation pressure inlet stream into a high stagnation pressure outlet stream and a low stagnation pressure outlet stream. The NASA Lewis Research Center three-port wave rotor experiment (cf. Wilson and Fronek, 1993) was simulated by a computation involving the medium pressure inlet port, the high pressure outlet port, and 39 rotor passages (see Fig. 4). The initial conditions in the passage about to open to the medium pressure port are set using a 1-D calculation courtesy of D. E. Paxson (see Paxson, 1993) and contain the "history" of the unsimulated portion of the cycle, including the impact of leakage. The two ports can be characterized by the ratio of the high pressure discharge mass flow rate to the inlet port mass flow rate and the ratio of average total pressures in these ports. Given the inlet port stagnation conditions and outlet port static conditions from the experiment, the code predicted mass flow rate fraction and pressure ratio of 0.346 and 1.193, respectively, while the experimental data showed a 0.371 mass flow rate fraction and 1.195 pressure ratio. The agreement in these machine performance variables is considered very good. Computed and measured total

velocity tangential distributions in the inlet port region of the experiment are compared in Fig. 5. The measurements were taken approximately 1 inch (2.5 cm) upstream of the rotor blades. The comparison shows excellent agreement between the experimental and computed velocities, including the inflection caused in part by the rounding of the leading port wall, near the rotor/port interface. The inlet port rounding effects a flow area increase which decelerates the flow just upstream of the rotor as indicated by the increase in the density contour levels (see Fig. 4). Also evident in Fig. 4 is that the density of the fluid entering the rotor decreases abruptly at the rotor interface as a result of the sudden decrease in flow area caused by the 7.4% blade blockage.

FOUR-PORT WAVE ROTOR APPLICATION

A simulation of the design-point operation of a planned four-port wave rotor experiment is discussed in this section. The four-port experiment calls for an external heater to add the energy that, in practice, is added in the burner of a gas turbine engine. The heater and four-port wave rotor combine to effect a Brayton cycle in which the rotor provides pressure gain (i.e., the exhaust port total pressure is higher than the inlet port total pressure) while producing zero net work by design. Only the wave rotor is modeled in the present work. The heat addition and heater pressure drop are implicit in the specified boundary conditions. Cycle timing and rotor dimensions were set by Paxson's (1995) 1-D code and the rotor optimization scheme described by Wilson and Paxson (1995). The wave rotor has one cycle per rotor and 30 passages per cycle. The rotor length is 10.5 inches (26.7 cm), the hub-to-tip ratio is 0.675, and the passage aspect (rotor length to blade-to-blade distance) ratio at the tip is 13.5. The rotor blade thickness is 8% of the blade-to-blade distance at mid-span. The rotor tip speed is 367 ft/s (112 m/s) at 10,500 rpm. The design mass flow rate is 1.45 lb_m/s (0.658 kg/s) at an exhaust port total temperature to inlet port total temperature ratio of 2.0, with inlet port conditions of 400 R (222 K) and 1 atm (0.101 MPa).

Calculation

Each rotor passage is discretized by a 115×41 H-grid with spacing adjacent to the blades of 3.5×10^{-3} inches (8.9×10^{-3} cm). The grid is stretched in the tangential-direction to provide gradual transition to 2.5×10^{-2} inch (6.4×10^{-2} cm) cell spacing near the passage centerline. The inlet and outlet port flow fields are each solved on 85×151 sheared H-grids, except for the low pressure exhaust port which is solved on a 85×165 grid. The same 3.5×10^{-3} inch (8.9×10^{-3} cm) near-wall grid spacing is used. The port and rotor grids are also stretched in the axial direction to provide gradual transition between the 2.5×10^{-2} inch (6.4×10^{-2} cm) spacing at the port/rotor interfaces and the 0.1 inch (0.25 cm) spacing of the interior cells. The inlet port leading wall is rounded at the port/rotor interface. The high pressure port has a rounding radius of 0.33 inches (0.84 cm) and the low pressure inlet port has a rounding of 0.2 inches (0.51 cm). The inlet and outlet port angles are set using the mean axial velocities from the 1-D design code and the specified rotor speed. A Reynolds number of 0.8295×10^6 /inch (0.3266×10^6 /cm) is prescribed for the low pressure inlet port reference conditions of 400 R (222 K) and 1 atm (0.101 MPa). The boundary conditions are also obtained from a 1-D design-point calculation, although in the course of the simulation the high pressure (to-heater) exhaust port back pressure is adjusted to

enforce equal mass flow rates in the low pressure ports. The 2-D calculation requires approximately a cpu-month on the Cray-YMP.

Flow Mechanics

An "unwrapped" view of the wave rotor solution is provided in Figs. 6 and 7 which show instantaneous total pressure and total temperature contours for the time-periodic (converged) solution. Time-averaged mixed-out port total properties are also noted. At the instant in time shown, the lowest passage is beginning to open to the low pressure exhaust port where, in this discussion, "low pressure" refers to the bottom two ports and "high pressure" refers to the top two ports.

Low pressure ports. The low pressure port region serves to draw unheated, relatively cold air on-board the rotor from the inlet port and to expand and discharge high pressure, high temperature passage fluid to the exhaust port. As a passage gradually opens to the low pressure exhaust port, an expansion fan moves into the passage and reduces the on-board pressure as the passage content is discharged to the exhaust port. The principal fan traverses the passage, reflects off the inlet port side of the rotor, and returns to the exhaust port. This is evident in the low pressure of the preceding passages. The passages are timed to open to the inlet port flow just as the static pressure in the rotor passage at the rotor/passage interface equals the inlet port relative total pressure. The inlet port flow is drawn onto the rotor as the fan establishes a negative (axial and tangential) pressure gradient at the rotor/inlet port interface. Figure 7 shows that the interface between the cold inlet port flow and the hot exhaust port flow is skewed: The principal expansion wave/interface interaction is a Rayleigh-Taylor flow. A radial baroclinic torque is established (i.e., radial vorticity is deposited) along the interface which is unstable to the acceleration established by the fan. The interface skews partly because of this baroclinic torque. The interface skewing is also likely affected by the velocity field induced by the vortices created as each passage gradually closes-off to the high pressure inlet port (see discussion below). As the right running once-reflected fan reaches the rotor/exhaust port interface, it reflects as left running compression waves off the (relatively uniform static pressure surface at the) rotor/exhaust port interface. As the fan reflects, the axial velocity at the rotor/exhaust port interface is reduced inversely with time (or tangential position), ideally to zero as the exhaust port ends. Non-uniformities caused by the fan, the rotor wakes, and the gradual opening of passages to the exhaust port lead to the (instantaneous) axial velocity profile shown in Fig. 8. The non-uniform velocity (or total pressure) profile effectively leads to mixing losses in the port. The compression waves generated by the twice-reflected expansion wave coalesce as they traverse the rotor back to the inlet port. Significant skewing of the cold/hot air interface occurs as the shock formed by the coalesced waves interacts with the interface. This Richtmeyer-Meshkov interaction results in vorticity deposition at the already distorted interface evidenced by the subsequent evolution of the interface. The inlet port ends (is "closed") as the coalesced shock in each passage reaches the rotor/inlet port interface. A pair of fairly strong counter-rotating vortices is created as each passage gradually closes-off from this port.

High pressure ports. The high pressure port region provides the main compression of the unheated air that enters the rotor in the low pressure inlet port. This gas, already slightly compressed by the

coalesced shock wave of the low pressure port region, is compressed another three to four times in the high pressure port region. As a passage gradually opens to the high pressure inlet (from-heater) port, compression waves—eventually steepening into a shock wave—move on-board, and compress and set into motion the on-board "driven" gas. This allows the incoming "driver" gas to enter the rotor passage. Simultaneously, an expansion wave moves into the port and reduces the total pressure and temperature of the incoming driver gas. Figure 9 shows a close-up of instantaneous density contours and velocity vectors during passage charging process. The evolution of the hot driver gas/cold driven gas interface is influenced by the local relative velocity which is effected by the inlet port rounding and blade profiling (after Keller, 1984, and see Welch, 1993). Note that a pocket of driven gas is captured by the driver gas due to incidence at the passage leading edge during opening. The principal shock traverses the rotor passage and reflects off the end-wall just as the high pressure exhaust (to-heater) port begins. The left-running reflected (λ) shock interacts strongly with the boundary layer established by the principal shock. The principal shock interacts with the cold-gas/hot-gas interface established earlier as the cold gas entered the low pressure inlet port. The reflected shock interacts with both this interface and the interface between the high pressure driver gas and cold driven gas. These Richtmeyer-Meshkov interactions impact the vorticity along the interfaces. The cold driven gas and the hot gas that was not discharged during the low pressure exhaust process, now compressed by both the principal and reflected shock waves, are discharged to the stratified exhaust port. The high pressure inlet port ends as the reflected shock arrives back at the inlet port/rotor interface. As a passage gradually closes-off from the inlet port, a pair of strong vortices is created, and an expansion fan is initiated which eventually brings the passage flow to rest in the rotor frame. The fan traverses the passage and brings the axial velocity at the rotor/exhaust port interface to zero, and is reflected in a manner similar to the fan in the low pressure exhaust port. In the presented simulation, the axial velocity in fact does not quite reach zero; a weak hammer shock merges with the coalescing wave produced as the fan reflects off the exhaust port. This wave can be barely discerned in Fig. 6 as it traverses, and is emitted from, the rotor during the low pressure exhaust port discharge process (as noted in Fig. 8).

Impact of Two-Dimensional Effects

The flow discharged to the heater is highly stratified (see Fig. 7), composed of both the cold air originally from the low pressure inlet port and the hot air not discharged in the low pressure exhaust process. In a gas turbine generator application, the hot air (exhaust gas recirculation) is previously burned. This hot gas is twice-compressed and is the hottest fluid in machine. Its entropy is that of the burner exhaust gas, plus that produced in the low pressure port region, plus that produced during recompression by the principal and reflected shocks back up to the peak cycle (to-heater) pressure. The 2-D total temperature contours of Fig. 7 illustrate that the particular (through-flow) four-port cycle simulated here creates high wall temperatures in the high pressure exhaust port.

Figure 7 shows that hot driver gas coats the trailing end of the high pressure exhaust port: More hot gas is discharged to the heater than anticipated by the 1-D design analysis. At the same time, the

captured cold (driven) air which by design was to be exhausted to the heater remains on-board the rotor and is discharged instead to the low pressure exhaust port. Exhaust port temperature non-uniformity is thus increased and less fresh air is discharged to the heater (burner) than intended. This redistribution (capturing) of cold and hot air is caused by the asymmetric gradual opening of passages to the high pressure inlet port and the subsequent evolution of the interface between the hot driver (from-heater) gas and cold driven gas. The redistribution accounts for a discrepancy between the actual 1.91 temperature ratio effected by the specified boundary conditions and the 2.0 temperature ratio effected by the same boundary conditions in the 1-D design code. Figures 6 and 7 show that the low pressure exhaust port is nonuniform in both total temperature and total pressure, in part due to this redistribution. Further, the trailing wall of the high pressure exhaust port is washed by hot fluid rather than cold, leading to higher duct wall thermal loads than projected by the initial 1-D design.

In addition to redistribution caused by the passage gradual opening process, redistribution of cold and hot gas occurs by interface skewing (discussed earlier) and by boundary layer dynamics; the latter leads to an inversion in the expected rotor blade (adiabatic) temperature profile. Figure 10 shows that the time-averaged free-stream (passage centerline) gas temperature is lower on inlet end of the wave rotor than on the outlet end. This is expected because cold flow enters, and spends the greatest fraction of the cycle time, on the inlet end of the rotor. Strictly 1-D analysis will suggest that the wall temperature distribution qualitatively follows the mean free-stream temperature; however, the predicted mean adiabatic wall temperature distribution of this work suggests that the wall temperature is higher on the inlet end of the rotor than the outlet end, and that the wall temperature gradient is reduced in magnitude from that of the free stream. The time-averaged adiabatic wall temperature—i.e., the time-averaged temperature of the boundary layer fluid adjacent to the wall—reflects the time-dependent boundary layer temperature distribution rather than the free-stream temperature distribution. Indeed, the entering cold flow moves over the hot boundary layer fluid attached to the rotor rather than displacing it as assumed in 1-D analysis. Similarly, at the discharge end of the rotor, some of the cold fluid remains in the boundary layers rather than being discharged to the high pressure exhaust port (heater). As a result, the mean rotor adiabatic wall temperature is lower than the mean free-stream temperature. The mean time-averaged free-stream temperature is near the averaged low pressure exhaust port total temperature whereas the mean time-averaged wall temperature is more like the colder exhaust port mixed-out static temperature. There is a hot spot at the inlet end of the rotor. The rotor wall temperature distribution will in general affect rotor design through thermal growth, stress, and (in some applications) rotor cooling considerations.

Machine Performance Levels

Wave rotor performance levels are compared in Fig. 11 in terms of the ratio of the low pressure exhaust and inlet port mixed-out total pressures versus the ratio of total temperatures in the same ports as predicted by the present work and by the 1-D design/analysis code (Paxson, 1995). The 2-D results are extrapolated through the anticipated experimental operating range using the 2-D predicted pressure ratio of 1.12 at the temperature ratio of 1.91 with a scaling that preserves the ratio of 2-D and 1-D CFD predicted pressure gains

(i.e., pressure ratio minus one) at the 1.91 temperature ratio. The 2-D extrapolated performance shows a 1.15 pressure ratio at the design-point temperature ratio of 2.0 rather than a 1.18 pressure ratio predicted by the 1-D CFD code. The differences between the 2-D calculations and the 1-D model are in part due to two-dimensional effects including entropy production in shock/boundary layer interactions and rotor wakes. Figure 11 indicates that the performance predicted by the 2-D solver is consistent with that reported by General Electric (cf. Mathur, 1985) and better than that reported by Rolls-Royce (cf. Moritz, 1985).

A second 2-D design-point simulation was carried out for a version of the four-port wave rotor in which the high pressure (from-heater) inlet port leading wall is not rounded; rather, the inlet port and stator end-wall form a sharp corner off which flow separates during the passage gradual opening process. As indicated in Fig. 11, the impact of inlet port rounding on wave rotor pressure gain is found to be negligible, contrary to suggestions in the literature (e.g., see Keller, 1984).

SUMMARY

A 2-D (θ, z), thin-layer Navier-Stokes solver developed to simulate unsteady, two-dimensional flow in the stator/rotor/stator geometry of multi-port wave rotors was described. Good agreement between computed results and three-port wave rotor experimental measurements was shown. The model was used to predict the design-point performance level of a planned four-port wave rotor experiment. The predicted performance is lower than that predicted by the 1-D code used to design the experiment, in part due to entropy production in separated flows in (λ) shock/boundary layer interaction and in the rotor blade wakes. Other important two-dimensional flow features were identified: skewing of the interface between hot and cold gases is caused by unstable Rayleigh-Taylor flows established by shock/contact (Richtmeyer-Meshkov) and expansion fan/contact interactions; vortices are created during passage gradual opening and closing processes and can influence the evolution of the cold gas/hot gas interfaces. Interface skewing, boundary layer flow dynamics, and passage gradual opening lead to the redistribution of hot and cold gas within the wave rotor passages in ways not accounted for by 1-D codes. The two-dimensional redistribution of hot and cold gas in the rotor impacts rotor blade and duct wall thermal loads. The impact of redistribution of hot and cold gas can be reduced by minimizing the relative amount of cold driven gas "captured" behind the hot driver gas during passage charging process in the high pressure port; this suggests increasing the rotor passage aspect ratio beyond the optimum determined by 1-D design analysis. Finally, a comparison of computations with straight and rounded inlet port leading walls showed that rounding affords no appreciable performance benefit.

ACKNOWLEDGEMENTS

Parts of this work were done while the author held a National Research Council-NASA LeRC Research Associateship. The author is grateful for the generous encouragement and technical support offered during the course of this work by NASA LeRC Turbomachinery Technology branch members Dr. Lawrence J. Boher, Dr. Rodrick V. Chima, and Dr. Jack Wilson (NYMA, Inc.) and System Dynamics branch member Dr. Daniel E. Paxson.

REFERENCES

- Anderson, W. K., Thomas, J. L., and van Leer, B., 1986, "Comparison of Finite Volume Flux Vector Splittings for the Euler Equations," *AIAA J.*, **24**, No. 9, September, pp. 1453-1460.
- Azoury, P. H., 1965-66, "An Introduction to the Dynamic Pressure Exchanger," *Proc. Inst. Mech. Eng.*, **180**, Part 1, pp. 451-480.
- Baldwin, B. S. and Lomax, H., 1978, "Thin-Layer Approximation and Algebraic Model for Separated Turbulent Flows," *AIAA-78-257*, Jan.
- Burri, H. U., 1958, "Non-Steady Aerodynamics for the Complex Supercharger," *ASME-58-GTP-15*, Mar.
- Chima, R. V., 1987, "Explicit Multigrid Algorithm for Quasi-Three-Dimensional Viscous Flows in Turbomachinery," *J. of Propulsion and Power*, **3**, No. 5, Sept.-Oct., pp. 397-405.
- Eidelman, S., 1985, "The Problem of Gradual Opening in Wave Rotor Passages," *J. Propulsion and Power*, **1**, No. 1, Jan.-Feb., pp. 22-28.
- Grossman, B. and Walters, R. W., 1989, "Flux-Split Algorithms for the Multi-Dimensional Euler Equations with Real Gases," *Computers and Fluids*, **17**, No. 1, pp. 99-112.
- Harten, A. and Hyman, J. M., 1983, "Self Adjusting Grid Methods for One-Dimensional Hyperbolic Conservation Laws," *J. Comp. Phys.*, **50**, pp. 235-269.
- Hong-De, J., 1983, "Two-Dimensional Unsteady Flow in Complex Rotor," *Proc. 1983 Tokyo International Gas Turbine Congress*, Oct., pp. 463-470.
- Jameson, A., Schmidt, W., and Turkel, E., 1981, "Numerical Solutions of the Euler Equations by Finite Volume Methods using Runge-Kutta Time-Stepping," *AIAA-81-1259*, June.
- Keller, J. J., 1984, "Some Fundamentals of the Supercharger Complex," in Sladky, 1984, pp. 47-54.
- Kenfield, J. A. C., 1969, "The Performance of Pressure-Exchanger Dividers and Equalizers," *J. Basic Engineering*, Sept., pp. 361-370.
- Larossiliere, L. M., 1995, "Wave Rotor Charging Process: Effects of Gradual Opening and Rotation," *J. Propulsion and Power*, Technical Note, **11**, No. 1, Jan.-Feb., pp. 178-184.
- Lear, W. E., Jr. and Candler, G., 1993, "Analysis of the Accuracy of Wave Rotor Boundary Conditions Using a Novel Computational Method," *AIAA-93-2524*, June.
- Mathur, A., 1985, "A Brief Review of G.E. Wave Engine Program (1958-1963)," in Shreeve and Mathur, 1985, pp. 171-193.
- Moritz, R., 1985, "Rolls-Royce Study of Wave Rotors 1965-1970," in Shreeve and Mathur, 1985, pp. 116-124.
- Paxson, D. E., 1993, "An Improved Numerical Model for Wave Rotor Design and Analysis," *AIAA-93-0482*, Jan.; also NASA TM-105915.
- Paxson, D. E., 1995, "Comparison Between Numerically Modeled and Experimentally Measured Wave-Rotor Loss Mechanisms," *J. Propulsion and Power*, **11**, No. 5, Sept.-Oct., pp. 908-914; also NASA TM-106279.
- Roe, P. L., 1981, "Approximate Riemann Solvers, Parameter Vectors, and Difference Schemes," *J. Comp. Phys.*, **43**, pp. 357-372.
- Rose, P. H., 1979, "Potential Applications of Wave Machinery to Energy and Chemical Processes," Lifshitz, A. and Rom, J., eds., *Shock Tubes and Wave*, *Proc. 12th Int. Symposium on Shock Tubes and Waves*, The Magnes Press, Jerusalem, Israel, July, pp. 3-30.
- Shreeve, R. P. and Mathur, A., eds., 1985, *Proc. 1985 ONR/NAVAIR Wave Rotor Research and Technology Workshop*, Report NPS-67-85-008, Naval Postgraduate School, Monterey, CA, May.
- Sladky, J. F., Jr., ed., 1984, *Machinery for Direct Fluid-Fluid Energy Exchange*, AD-07, Winter Annual Meeting of The ASME, New Orleans, LA, Dec. 9-14.
- Sturtevant, B., 1987, "Rayleigh-Taylor Instability in Compressible Fluids," Gronig, H., ed., *Shock Tubes and Waves*, *Proc. of the Sixteenth Int. Symp. on Shock Tubes and Waves*, Aachen, West Germany, July, VCH, Federal Republic of Germany, pp. 89-100.
- Taussig, R. T., 1984, "Wave Rotor Turbofan Engines for Aircraft," in Sladky, 1984, pp. 9-45; also see *Mech. Engineering*, Nov., 1984, pp. 60-66.
- Taussig, R. T. and Hertzberg, A., 1984, "Wave Rotors for Turbomachinery," in Sladky, 1984, pp. 1-7.
- Thayer, W. J., III, Vaidyanathan, T. S., and Zumdieck, J. F., 1980, "Measurements and Modeling of Energy Exchanger Flow," *Proc. Intersociety Energy Conversion Engineering Conference*, **3**, Aug., pp. 2368-2379.
- van Leer, B., 1979, "Towards the Ultimate Conservative Difference Scheme. V. A Second-Order Sequel to Godunov's Method," *J. Comp. Phys.*, **32**, pp. 101-136.
- Walters, R. W. and Thomas, J. L., 1989, "Advances in Upwind Relaxation Methods," Noor, A. K. and Oden, J. T., eds., *State-of-the-Art Surveys on Computational Mechanics*, The American Society of Mechanical Engineers, New York, U.S.A., pp. 145-183.
- Welch, G. E., 1993, "Two-Dimensional Numerical Study of Wave Rotor Flow Dynamics," *AIAA-93-2525*, June.
- Welch, G. E. and Chima, R. V., 1993, "Two-Dimensional CFD Modeling of Wave Rotor Flow Dynamics," *Proc. 11th Computational Fluid Dynamics Conference*, Part 1, *AIAA-93-3318-CP*, July, pp. 234-247; also NASA TM-106261.
- Welch, G. E., Jones, S. M., and Paxson, D. E., 1995, "Wave Rotor-Enhanced Gas Turbine Engines," *AIAA-95-2799*, July; also NASA TM-106998 and ARL-TR-806.
- Welch, G. E., 1996, "Macroscopic Balance Model for Wave Rotors," *AIAA-96-0243*, Jan.; also NASA TM-107114 and ARL-TR-925.
- Wen, W. and Mingzheng, C., 1982, "Some Result (sic) of Theoretical Analysis, Calculation and Experimental Research of Pressure Wave Supercharger," *J. Engineering Thermophysics*, **3**, No. 1, Feb., pp. 33-38.
- Wilson, J. and Fronck, D., 1993, "Initial Results from the NASA Lewis Wave Rotor Experiment," *AIAA-93-2521*, June; also NASA TM-106148.
- Wilson, J. and Paxson, D. E., 1995, "Optimization of Wave Rotors for Use as Gas Turbine Engine Topping Cycles," *SAE-951411*, May; also NASA TM-106951.
- Zauner, E., Chyou, Y.-P., Walraven, F., and Althaus, R., 1993, "Gas Turbine Topping Stage Based on Energy Exchangers: Process and Performance," *ASME-93-GT-58*, May.
- Zehnder, G., 1971, "Calculating Gas Flow in Pressure-Wave Machines," *Brown-Broveri Review*, Rev. 4/5, pp. 172-176.
- Zhang, H.-S., 1988, "The Coordinate Splitting Solution of Euler-Lagrange for Treating Interfaces in Two-Dimensional Unsteady Flow," *AIAA-88-3563-CP*, pp. 92-97.

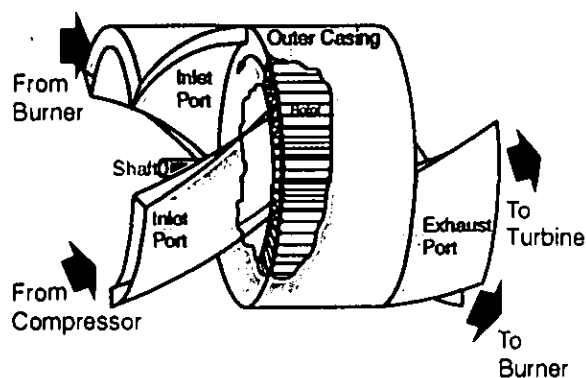


Figure 1. Four-port wave rotor schematic diagram.

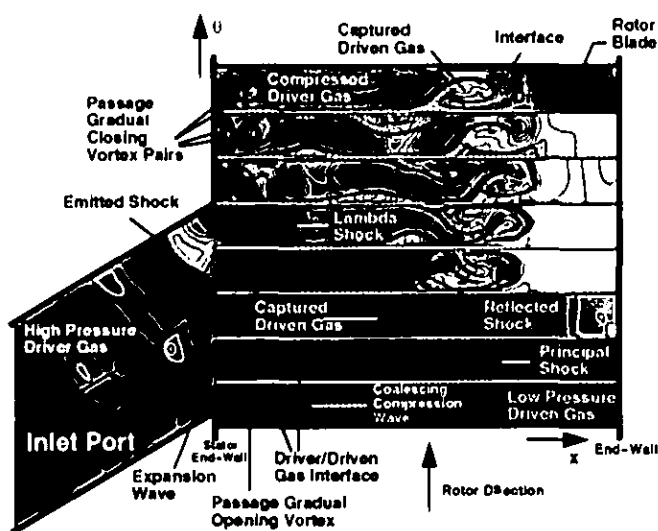


Figure 2. Prototypical inlet port/passage charging process showing computed density contours (Non-dimensional values: Dark blue = 0.6 and Magenta = 4.6.)

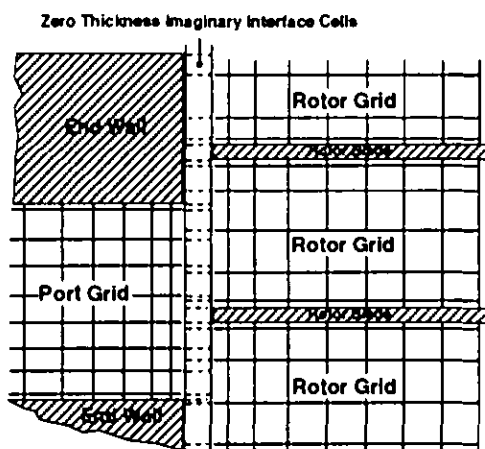


Figure 3. Schematic diagram of Instantaneous port/passage imaginary interface cell construction.

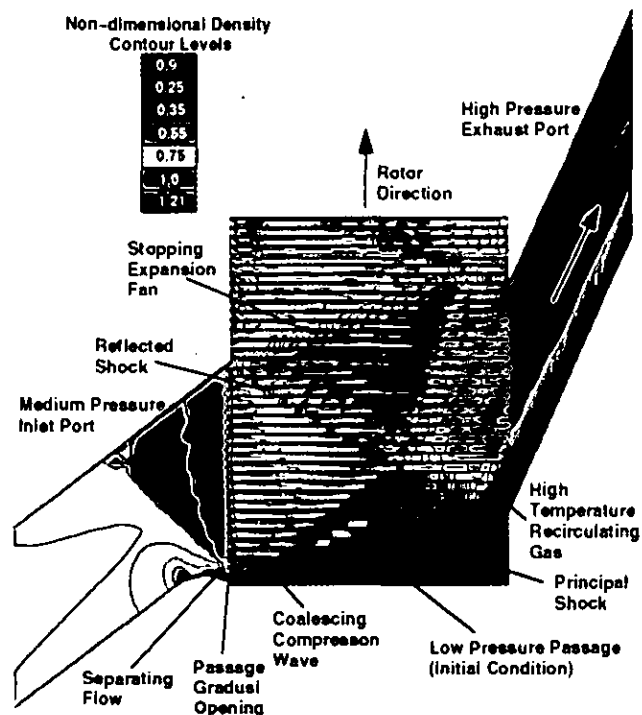


Figure 4. Computed instantaneous density contours in medium pressure inlet port and high pressure outlet port region of NASA LeRC three-port divider cycle experiment.

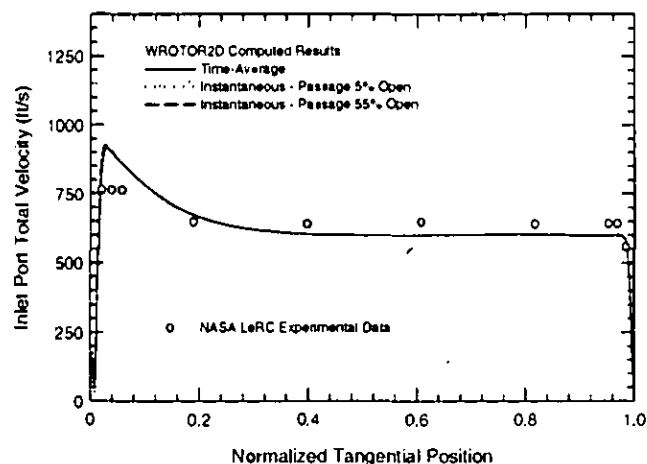


Figure 5. Comparison of computed and measured (Wilson and Fronek, 1993) NASA LeRC three-port divider cycle experiment medium pressure inlet port total velocity as a function of normalized tangential position.

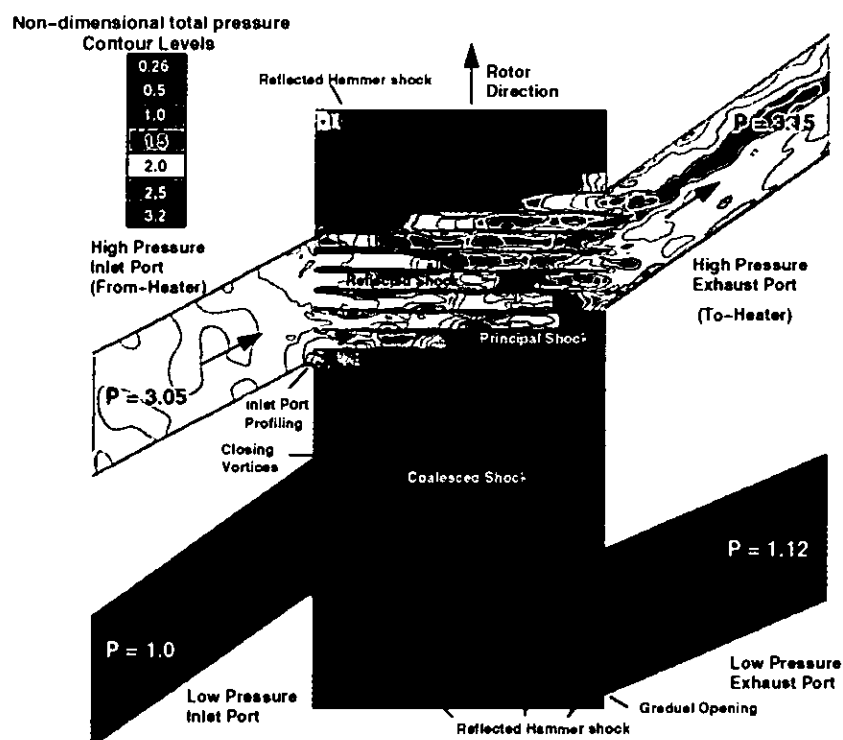


Figure 6. Computed instantaneous total pressure contours and normalized mixed-out port pressures of planned four-port wave rotor experiment.

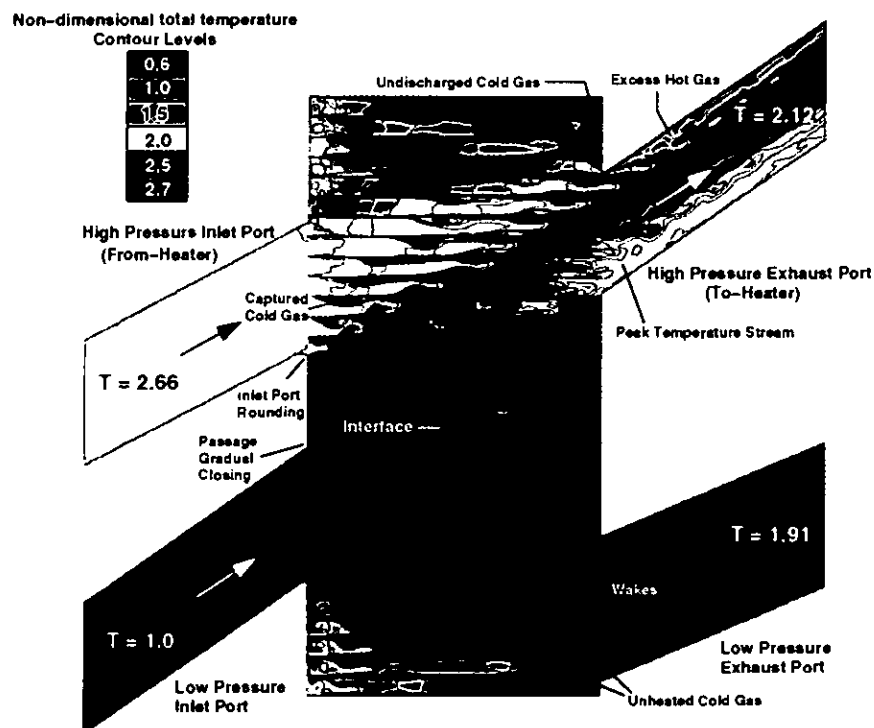


Figure 7. Computed instantaneous total temperature contours and normalized mixed-out port temperatures of planned four-port wave rotor experiment.

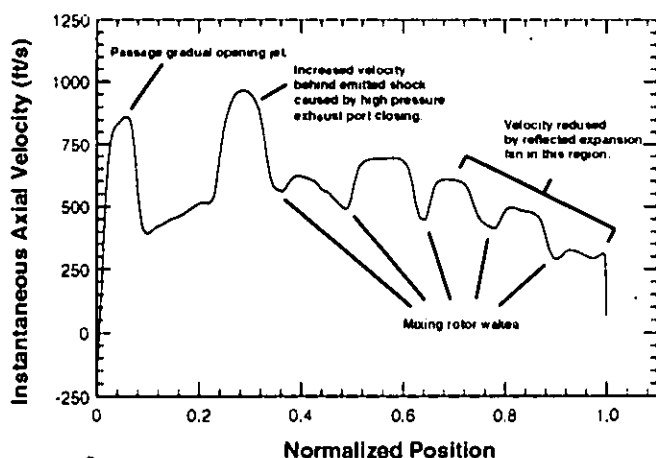


Figure 8. Computed instantaneous axial velocity as a function of position in low pressure exhaust port, one passage width from rotor face, showing features contributing to exhaust port non-uniformity.

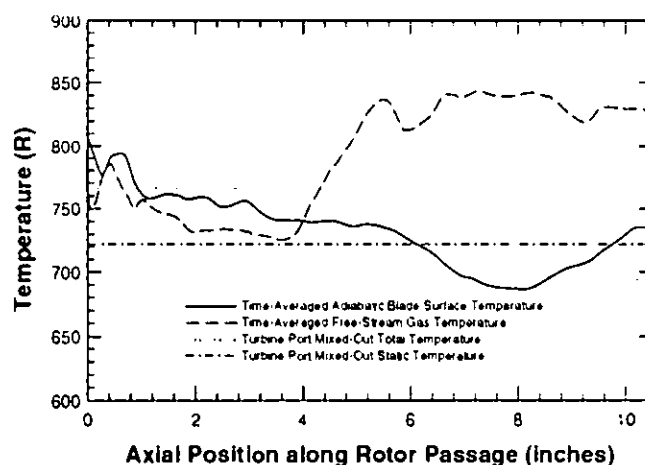


Figure 10. Comparison of computed axial distributions of time-averaged passage free-stream temperature and rotor blade surface temperature for planned NASA Lewis Research Center four-port wave rotor experiment at design point.

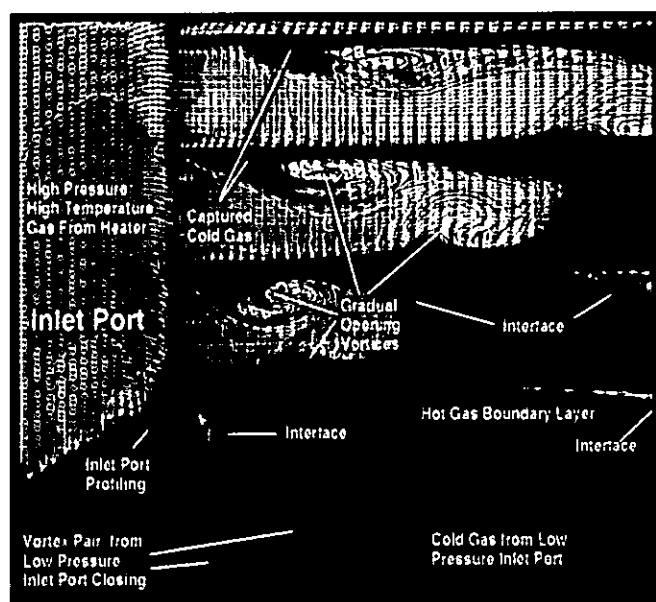


Figure 9. Computed instantaneous density contour and velocity vectors showing close-up view of passage gradual opening process and two-dimensional flow features contributing to redistribution of hot and cold gases.

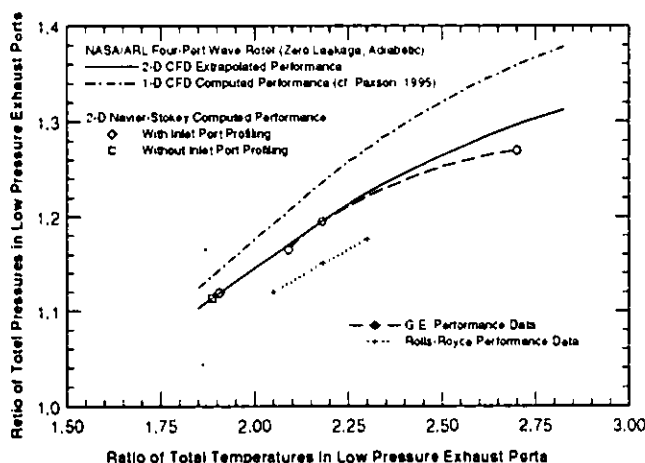


Figure 11. Comparison of computed performance of planned NASA Lewis Research Center four-port wave rotor with G.E. experimental data (reported by Mathur, 1985) and Rolls-Royce experimental data (reported by Moritz, 1985).